Eur. Phys. J. B **21**, 81–91 (2001)

THE EUROPEAN PHYSICAL JOURNAL B

EDP Sciences

Electron-doping versus hole-doping in the 2D t-t' Hubbard model

C. Honerkamp[a]

Theoretische Physik, ETH-Hönggerberg, 8093 Zürich, Switzerland

Received 19 December 2000 and Received in final form 28 February 2001

Abstract. We compare the one-loop renormalization group flow to strong coupling of the electronic interactions in the two-dimensional t-t'-Hubbard model with $t' = -0.3t$ for band fillings smaller and larger than half-filling. Using a numerical N-patch scheme ($N = 32, \ \ldots, \ 96$) we show that in the electron-doped case with decreasing electron density there is a rapid transition from a $d_{x^2-y^2}$-wave superconducting regime with small characteristic energy scale to an approximate nesting regime with strong antiferromagnetic tendencies and higher energy scales. This contrasts with the hole-doped side discussed recently which exhibits a broad parameter region where the renormalization group flow suggests a truncation of the Fermi surface at the saddle points. We compare the quasiparticle scattering rates obtained from the renormalization group calculation which further emphasize the differences between the two cases.

PACS. 71.10.Fd Lattice fermion models (Hubbard model, etc.) – 74.72.Jt Other cuprates

1 Introduction

Viewed from a weak coupling perspective, the two-dimensional Hubbard model exhibits an interesting interplay between different types of fluctuations. Particular attention has been devoted to the situation close to half band filling, mainly because of its relevance to the high-T_c superconducting cuprates [1]. For these particle densities, because of the approximate nesting between opposite sides of the Fermi surface (FS) or due to the large density of states around the saddle points of the dispersion at $(\pi, 0)$ and $(0, \pi)$, the scattering processes with momentum transfer $\approx (\pi, \pi)$ will be strongly enhanced. Besides the fact that these scattering processes drive antiferromagnetic (AF) fluctuations, they also create a $d_{x^2-y^2}$-wave component in the pair scattering [2]. One-loop renormalization group (RG) techniques represent a powerful method to analyze the coupling between antiferromagnetic and superconducting fluctuations in an unbiased way (see [3–11] and the present paper).

Apart from the competition between two different types of ground states, the hole-doped t-t' Hubbard model close to half filling may exhibit a richer variety of possible ground states especially when umklapp scattering between electrons becomes important. In [7] and [10] it was argued that in the case of not-too-small values of the next-nearest neighbor hopping t', *e.g.* $t' = -0.3t$, when the FS is close to the saddle points at $(\pi, 0)$ and $(0, \pi)$, the RG flow to strong coupling between the **k**-space regions around the saddle points has strong similarities with the RG flow in the half-filled two-leg Hubbard ladder. In the latter system, the ground state is well understood and is an insulating spin liquid (ISL) [12]. Although there is no reliable theory for the two-dimensional case, the similarity of the RG flows suggests that here as well the true strong coupling state of the **k**-space regions around the saddle points is an ISL with a truncated FS. The parameter region in which this interesting flow to strong coupling occurs was called the *saddle point regime*.

In this paper we investigate the RG flow to strong coupling for band fillings larger than half-filling, corresponding to electron-doping the half-filled system. Again we choose $t' = -0.3t$. The main observation is that in the electron-doped case the saddle point regime of the hole-doped case is absent. Instead of the mutually reinforcing flow between AF and d-wave pairing processes which was found in the saddle point regime, there is a clear separation between the energy scales of the two channels. We do not find any signs for a Fermi surface truncation around the saddle points. Moreover the "hot" Brillouin zone (BZ) regions responsible for the leading flow are now located closer to the BZ diagonals. The different result is a direct consequence of the location of the Fermi surface, which in the electron-doped case crosses the umklapp surface (US, defined in Fig. 4) in the BZ diagonal, therefore giving rise to strong scattering between the FS segments on opposite sides connected by the wave vector (π, π). These AF processes generate only a weak attractive $d_{x^2-y^2}$ component in the pair scattering channel and do not drive the pairing processes at low scales as they do in the saddle point regime of the hole-doped case. Consequently, upon increasing the band filling such that the (π, π) processes get cut off, we obtain a rather abrupt transition from a flow to strong coupling dominated by umklapp and AF processes with high critical scale to a Kohn-Luttinger-like instability

[a] e-mail: chonerka@itp.phys.ethz.ch

with predominant $d_{x^2-y^2}$-Cooper processes at comparably low critical scale. Therefore the electron-doped case considered here strongly resembles the hole-doped cases with small absolute values of t' analyzed in [6] and [8,9] and differs from the hole-doped case with $t' = -0.3t$ discussed in [10].

As another piece of information we present results for the scattering rates of quasiparticles at the FS with a RG method described below. These calculations further illustrate the differences between the hole- and electron-doped cases. According to model calculations by Ioffe and Millis [13] and also Hlubina [14] most transport experiments of the optimally hole-doped cuprates can be properly described by assuming a pronounced anisotropy in the scattering rate. The anisotropy is such that the quasiparticles around the saddle points scatter strongly and their spectral weight becomes smeared out while the quasiparticles in the BZ diagonal are only subject to a weak Fermi-liquid-like scattering. Our RG calculations with frequency-independent coupling constants can certainly not give reliable information about the frequency dependence of the self-energy. On the other hand their **k**-space resolution is rather good. Applying the RG scheme we observe a pronounced angular dependence of $\mathrm{Im}\,\Sigma(\mathbf{k}_\mathrm{F}, \omega = 0)$ with maximal scattering for particles at the saddle points and weaker scattering in the BZ diagonals. In the electron-doped case, the anisotropy is weaker and the FS regions with the largest scattering rate are located in the BZ diagonals, tied to the intersection of the FS with the US.

Angular resolved photoemission (ARPES) allows one to measure the temperature dependence of $\mathrm{Im}\,\Sigma(\omega = 0, \mathbf{k}_\mathrm{F})$ directly from the width of the quasiparticle peaks. For optimally hole-doped Bi 2212, Valla *et al.* [15] found a linear-T dependence almost everywhere on the FS. For a comparison we calculate the quasiparticle scattering rates at high temperatures, where the RG flow does not diverge. Our results for the hole-doped case are qualitatively similar to the experimental data. In the electron-doped case the RG calculations yield a non-linear T-dependence of the scattering rates closer to conventional T^2 behavior.

2 The method

Here we describe the RG method and the scheme for the calculation of the quasiparticle scattering rates. Readers who are only interested in the results can proceed to the next section.

2.1 RG flow of interactions and susceptibilities

The interplay between the different fluctuations mentioned in the introduction can be appropriately analyzed within one-loop RG where one successively integrates out intermediate states according to their band energy $\epsilon_\mathbf{k}$. For the two-dimensional Hubbard model on the square lattice with nearest neighbor hopping t and next-nearest neighbor hopping t',

$$\epsilon_\mathbf{k} = -2t\,(\cos k_x + \cos k_y) - 4t' \cos k_x \cos k_y - \mu,$$

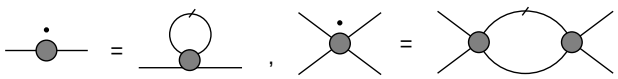

Fig. 1. The one-loop RG equations for two- and four-point vertex function. The dot symbolizes the derivative with respect to the energy scale Λ.

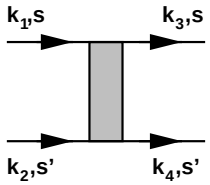

Fig. 2. The coupling function $V_\Lambda(\mathbf{k}_1, \mathbf{k}_2, \mathbf{k}_3)$. $\mathbf{k}_1, s$ $(\mathbf{k}_2, s')$ specify the first (second) incoming particle, $\mathbf{k}_3, s$ $(\mathbf{k}_4, s')$ belong to the first (second) outgoing particle.

where μ is the chemical potential and the lattice constant is set to unity.

The RG scheme for 1PI irreducible vertex functions which we use is explained and discussed in detail in reference [16]. Here we give simple graphical explanation of the RG flow for the two- and four-point vertex functions. The flow of higher order irreducible vertex functions is not taken into account.

The differential equations for the two-point vertex (yielding the scale-dependent self-energy $\Sigma_\Lambda(\mathbf{k}, \mathrm{i}\omega)$) and the four-point vertex function, which describe their RG flow with decreasing energy scale Λ, are described graphically in Figure 1. At the internal vertices we have four-point vertex functions at scale Λ connecting the incoming and outgoing lines with the internal ones. Crystal momenta and Matsubara frequencies are conserved at the vertices. One of the two internal lines corresponds to a so-called single scale propagator S_Λ which is only non-zero for modes at scale Λ while the other line denotes a full Green's function G_Λ with low energy modes below scale Λ cut out through a cutoff function $C(\Lambda, |\epsilon_\mathbf{k}|)$. Throughout this paper we neglect possible self-energy corrections, therefore we have

$$G_\Lambda(\mathbf{k}, \mathrm{i}\omega) = \frac{C(\Lambda, |\epsilon_\mathbf{k}|)}{\mathrm{i}\omega - \epsilon_\mathbf{k}} \quad \text{and} \quad S_\Lambda(\mathbf{k}, \mathrm{i}\omega) = \frac{\partial_\Lambda C(\Lambda, |\epsilon_\mathbf{k}|)}{\mathrm{i}\omega - \epsilon_\mathbf{k}}\,.$$

The scale-dependent spin-rotation invariant four-point vertex function $\Gamma_\Lambda(\mathbf{k}_1, s_1, \mathbf{k}_2, s_2, \mathbf{k}_3, s_3, \mathbf{k}_4, s_4)$ can be expressed in terms of a coupling function $V_\Lambda(\mathbf{k}_1, \mathbf{k}_2, \mathbf{k}_3)$ [10,16] which is determined for the case $s_1 = s_3$ and $s_2 = s_4$. The s_i denote the z-components of the spins of incoming (s_1 and s_2) and outgoing (s_3 and s_4) particles. $V_\Lambda(\mathbf{k}_1, \mathbf{k}_2, \mathbf{k}_3)$ is represented graphically in Figure 2. This means that the electron-electron interaction at energy scale Λ is a function of the two incoming wave vectors $\mathbf{k}_1$ and $\mathbf{k}_2$ and one outgoing wave vector $\mathbf{k}_3$. For the bare Hubbard interaction at starting scale $\Lambda_0 \approx 4t$, we set $V_{\Lambda_0}(\mathbf{k}_1, \mathbf{k}_2, \mathbf{k}_3) = U$. For all calculations in this paper we choose $U = 3t$. The flow of $V_\Lambda(\mathbf{k}_1, \mathbf{k}_2, \mathbf{k}_3)$ with decreasing the energy scale Λ is then given by all types of one-loop

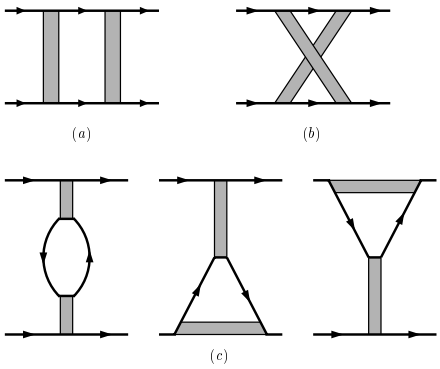

Fig. 3. The contributions to the right–hand side of the RG equation for the coupling function $V_\Lambda(\mathbf{k}_1, \mathbf{k}_2, \mathbf{k}_3)$, (a) the particle–particle term, (b) the crossed particle–hole term, (c) the direct particle–hole terms; the first of these three graphs gets a factor -2 because of the fermion loop.

diagrams including particle-particle and particle-hole diagrams with all possible momentum transfers (see Fig. 3).

For the numerical integration of these coupled equations we use a phase space discretization following Zanchi and Schulz [6]. The BZ is divided up into nN patches centered around N lines. Each line starts from the origin in a certain angular direction $\theta(k)$ and from the $(\pm\pi, \pm\pi)$-points so that the lines meet at the umklapp surface. The phase space segments around these lines are then further split into n patches. Here we took $n = 3$ where one patch per line is centered around the FS with *e.g.* $|\epsilon(\mathbf{k})| < 0.4t$, while the other two patches cover phase space regions at higher positive or negative band energy.

Then the coupling function is discretized as follows: we approximate $V_\Lambda(\mathbf{k}_1, \mathbf{k}_2, \mathbf{k}_3)$ by a constant for all wave vectors in the same patches and calculate the RG flow for the subset of interaction vertices with one wavevector representative for each patch. In the low energy patches around the FS we choose to take these wave vectors as the crossing points of the N lines with the Fermi surface (FS), the wave vectors for the remaining patches away from the FS correspond to a higher band energy, *e.g.* $|\epsilon(\mathbf{k})| = 0.8t$ (see Fig. 4). The phase space space integrations are performed as sums over the patches and integrations over the radial direction along 3 or 5 lines inside each patch. Most calculations were done using a 32×3 system, *i.e.* $N = 32$ and $n = 3$. Two typical Fermi surfaces with $N = 32$ points are shown in Figure 5.

Along with the flow of the interactions we calculate several static susceptibilities by coupling external fields of appropriate form to the electrons. During the flow these external coupling are renormalized through one-loop vertex corrections, as described in reference [10]. The pairing and AF susceptibilities can be calculated directly with the RG flow of the coupling function. The susceptibilities and couplings to uniform external charge and spin fields require special care as they only involve particle-hole excitations in a shell around the FS with width of the temperature. Before the cutoff Λ reaches that scale the interactions have typically grown larger than the bandwidth such that the one-loop flow is not reliable any longer. In order to get a qualitative result for these cases we stop the flow of the interactions at a certain scale $\Lambda_{\rm freeze}$ and treat them as constants in the continuation of the flow of the susceptibilities down to $\Lambda = 0$ where we obtain the main contributions to the uniform susceptibilities. This is basically equivalent to stopping the RG flow at $\Lambda_{\rm freeze}$ and calculating these susceptibilities for the effective theory below the cutoff $\Lambda_{\rm freeze}$ within RPA (random phase approximation) using the renormalized interactions given by the RG down to $\Lambda_{\rm freeze}$. A similar way to obtain the uniform susceptibilities from the flow of the Landau function has been used in reference [8].

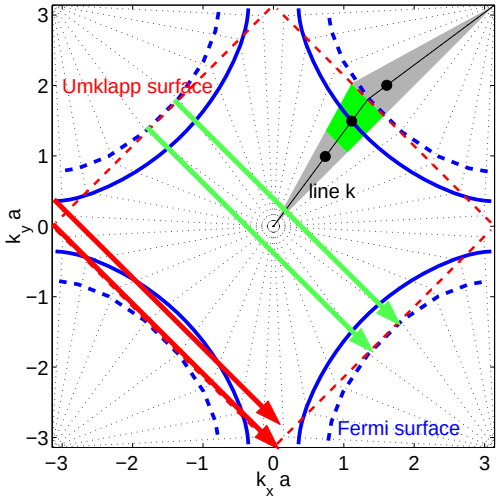

Fig. 4. The Brillouin zone, Fermi and umklapp surfaces and the lines in the patch centers for $N = 32$. The solid dots in the patches denote the wave vectors for which the four-point vertex function is calculated. For all wave vectors inside the same patch, $V_\Lambda(\mathbf{k}_1, \mathbf{k}_2, \mathbf{k}_3)$ is approximated by a constant. The solid line denotes the non-interacting FS for $t' = -0.3t$ and $\mu = -t$, which is in the saddle point regime of hole-doped case. The curved dashed line is a typical FS for the electron-doped case. The straight dashed lines connecting the $(\pm\pi, 0)$- and $(0, \pm\pi)$-points denote the umklapp surface. The arrows symbolize umklapp processes between the saddle point and the BZ diagonals, respectively.

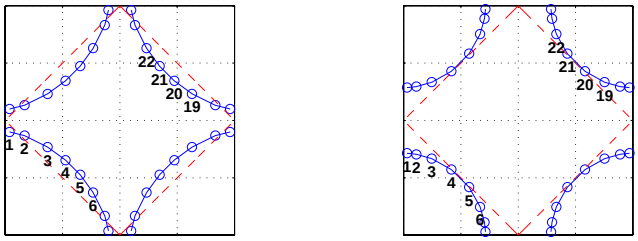

Fig. 5. The Fermi surfaces and $N = 32$ points $\mathbf{k}_{\rm F}(k_i)$ for which the coupling function $V_\Lambda(k_1, k_2, k_3)$ is calculated. Left plot: $\mu = -1.05t$ (hole-doped, $\langle n \rangle \approx 0.83$). Right plot: $\mu = 0$ (electron-doped, $\langle n \rangle \approx 1.2$ per site).

2.2 Approximate calculation of the scattering rates

Here we describe an approximation scheme for the calculation of the imaginary part of the self-energy from the flow of coupling function. The technical problem occurring in the RG formalism presented above is that we have neglected all frequency dependencies of the four-point vertex, hence the four-point vertex in the one-loop contribution to Σ at scale Λ in Figure 1 is a real quantity and the diagram does not give an imaginary part. This deficiency can be repaired to a large extent by replacing the approximate frequency-independent vertex with the solution of the one-loop RG equation for the four-point vertex in its integral form. This effectively yields a two-loop term corresponding to a two-particle–one-hole intermediate state which, after analytical continuation to real frequencies, gives a non-vanishing imaginary part. Moreover these contributions to $\mathrm{Im}\,\Sigma_\Lambda$ are the leading ones, because all neglected contributions from further insertions of one-loop diagrams at the vertices have intermediate states with a number of intermediate particles larger than 3 and can therefore be expected to give only small contributions due to phase space restrictions. If we ignored the flow of the coupling constants and integrated the expression thus obtained down to $\Lambda = 0$, we would retrieve the bare two-loop selfenergy. In this paper we neglect the feedback of the self-energy on the flow of the coupling function. In principal this effect is contained in the RG equations but keeping it would increase the complexity of the calculations considerably.

Formally we can calculate the selfenergy $\Sigma_{\Lambda=0}(\mathbf{k}_\mathrm{F}, \mathrm{i}\omega)$ at the FS for Matsubara frequency $\mathrm{i}\omega$ by integrating the RG differential equation for the scale-dependent selfenergy depicted in Figure 1 as follows:

$$\Sigma_{\Lambda=0}(\mathbf{k}_\mathrm{F}, \mathrm{i}\omega) = \int_{\Lambda_0}^{0} \mathrm{d}\Lambda \int \frac{\mathrm{d}^2 k'}{(2\pi)^2} \times \sum_{\mathrm{i}\omega'} \left[-2V_\Lambda(\mathbf{k}_\mathrm{F}, \mathbf{k}', \mathbf{k}_\mathrm{F}) + V_\Lambda(\mathbf{k}_\mathrm{F}, \mathbf{k}', \mathbf{k}')\right] S_\Lambda(\mathbf{k}', \mathrm{i}\omega').$$

For V_Λ we now substitute the differential equation for the four-point vertex, integrated from the starting scale Λ_0 down to Λ. This corresponds to inserting the one-loop diagram on the right side of Figure 1 into the self-energy graph on the left side. Then we get a second integral over $\mathrm{d}\Lambda'$:

$$\Sigma_{\Lambda=0}(\mathbf{k}_\mathrm{F}, \mathrm{i}\omega) = \int_{\Lambda_0}^{0} \mathrm{d}\Lambda \int_{\Lambda_0}^{\Lambda} \mathrm{d}\Lambda' \sum V_{\Lambda'} G_{\Lambda'} S_{\Lambda'} S_\Lambda V_{\Lambda'}. \tag{1}$$

Here the sum is over all internal wavevectors, frequencies and spin indices of the different possible diagrams. For simplicity we have suppressed the arguments of the four-point vertices and propagators in this expression. Obviously, repeating the insertion of scale-integrated one-loop terms for the vertices yields a perturbation expansion of the self-energy with arbitrary numbers of intermediate states. Here we restrict the analysis to the contributions

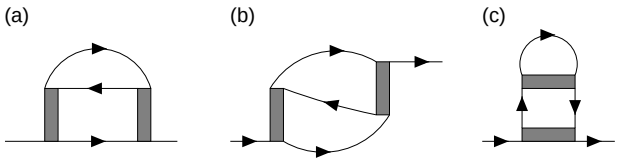

Fig. 6. The different diagrams for the two-loop self-energy. Diagrams (a) and (b) contribute to the imaginary part of the self-energy, contributions of type (c) are real for external frequency $\omega + \mathrm{i}\delta$. There are 3 other diagrams of type (c) with different orientation of the vertices which are not shown here.

from the two-loop term (1), which contains the Landau-Fermi liquid self-energy and the deviations from it through the flow to strong coupling of the coupling function V_Λ.

In the integrand in (1), the two four-point vertices $V_{\Lambda'}$, one single scale propagator $S_{\Lambda'}$ and one full propagator $G_{\Lambda'}$ depend on Λ'. The only Λ-dependence is in the differentiated cutoff-function $\dot{C}(\Lambda)$ of the original single-scale propagator S_Λ. Therefore (1) has the structure

$$\Sigma_{\Lambda=0}(\mathbf{k}_\mathrm{F}, \mathrm{i}\omega) = \sum \int_{\Lambda_0}^{0} \mathrm{d}\Lambda \dot{C}(\Lambda) \int_{\Lambda_0}^{\Lambda} \mathrm{d}\Lambda'\ R(\Lambda').$$

The double scale integral is numerically expensive, but we can circumvent it by a partial integration, resulting in

$$\Sigma_{\Lambda=0}(\mathbf{k}_\mathrm{F}, \mathrm{i}\omega) = \sum \int_{\Lambda_0}^{0} \mathrm{d}\Lambda \left[C(0) - C(\Lambda)\right]\ R(\Lambda). \tag{2}$$

The remainder $R(\Lambda)$ contains one single scale propagator at Λ and a propagator for modes above Λ. The difference of cutoff functions in the rectangular brackets means that the third of the three internal lines has its support on modes below the cutoff. The form (2) only contains a single Λ-integral and the vertex functions at Λ. Therefore it can be integrated along with the flow of the four-point vertex. Note however that for consistency with (1) we should always integrate out the full scale range.

Diagrammatically the insertion of the one-loop flow into the one-loop diagram for the self-energy yields three topologically different diagrams which are shown in Figure 6. Each of these three diagrams gives 6 contributions: one of the internal line contains modes above Λ, another modes at Λ, and the third below Λ.

Since we are interested in the quasiparticle scattering rates, we perform an analytical continuation onto the real frequency axis: the integrand of the two diagrams (a) and (b) in Figure 6 contains the factor

$$\frac{1}{\mathrm{i}\omega - \epsilon_1 - \epsilon_2 + \epsilon_3}$$

which upon replacing $\mathrm{i}\omega \to \omega + \mathrm{i}\delta$ with $\omega = 0$ yields an imaginary part $\propto \delta(\epsilon_1 + \epsilon_2 - \epsilon_3)$. The δ-function is smeared with a small width for the numerical treatment.

One can show that for scale-independent vertices, *e.g.* all $V_\Lambda(\mathbf{k}_1, \mathbf{k}_2, \mathbf{k}_3) = U$, this scheme is equivalent to the calculation of the bare two-loop diagram. Thus for ordinary cases where the flow does not diverge we should obtain

two-dimensional Fermi-liquid results. In our case the flow goes to strong coupling, and this leaves two possibilities for the analysis: either we choose a high temperature such that the couplings do not become too large, then we can apply the above scheme down to zero scale and obtain an estimate for the imaginary part of the self-energy above the strong coupling phase. The other option is, if we want to analyze the situation in the strong coupling regime, to stop the flow of the couplings at some scale $\Lambda_{\rm freeze}$ and integrate the flow down to zero scale with fixed couplings. We can then vary $\Lambda_{\rm freeze}$ and thus obtain the change in the imaginary part of the self-energy due to the flow of the couplings. This will tell us on which FS parts the renormalized interactions weaken the quasiparticles most and we will *e.g.* find that in the hole-doped case the quasiparticles in the BZ diagonals are not affected by strong scattering. The results of both types of analysis are described in Section 6.

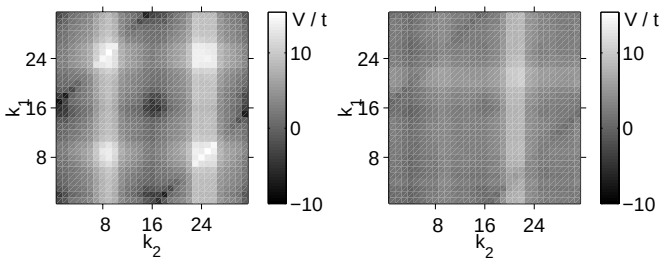

Fig. 7. Snapshot of the RG flow when the couplings have reached values larger than the bandwidth for the hole-doped case in the saddle point regime, $t' = -0.3t$ and $\mu = -t$. The color bar denotes the value of the couplings $V(k_1, k_2, k_3)/t$, where $\mathbf{k}_{\rm F}(k_1)$ and $\mathbf{k}_{\rm F}(k_2)$ are the two incoming wavevectors on the FS and the outgoing wavevector $\mathbf{k}_{\rm F}(k_3)$ is fixed at point 1 or 4. The 32 points are numbered according to their position around the FS, points 1, 8, 9, 16, etc. are closest to the saddle points.

3 Comparison of the flows to strong coupling

First we compare the RG flow of the interactions. For the chosen parameters we generally find a flow to strong coupling, *i.e.* at sufficiently low scales and temperatures some components of the coupling function $V_\Lambda(k_1, k_2, k_3)$ take absolute values larger than the band energy. We analyze the flow to strong coupling at scale Λ_W where the coupling functions just exceed the order of the bare bandwidth, *i.e.* at $V_{\Lambda_W,\max} \approx 8 - 12t$. At these scales and for typical temperatures, the coupling functions have already developed a pronounced **k**-space structure and the dominant interaction terms at this scale will certainly be important for the strong coupling state. On the other hand the FS shift due to one-loop self-energy corrections is still small [10] such that it does not qualitatively change the flow above Λ_W. Similarly the scattering rate for particles at the FS (see below) remains smaller than Λ_W. Note however that at Λ_W and for initial interaction $U = 3t$ the flow has not reached an asymptotic form and different classes of coupling constants would evolve differently if we continued the flow below Λ_W (where our method breaks down). Therefore the analysis of the flow to strong coupling remains qualitative and does not provide definitive conclusions about the true strong coupling state.

3.1 Hole-doped model

The hole-doped case with $t' = -0.3t$ was extensively discussed in reference [10]. In order to simplify the comparison with results for the electron-doped case we repeat the main observations briefly. We found that in the density region where the FS crosses the US close to the saddle points the dominant processes which grow fastest upon integrating out higher energy modes are given by mutually reinforcing umklapp and Cooper processes between the saddle point regions. This leads to a flow to strong coupling at relatively high critical scales. The scattering processes involving quasiparticles in the BZ diagonals grow

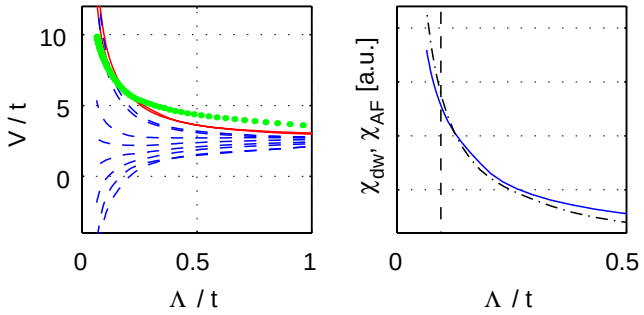

Fig. 8. Flow of certain coupling functions and susceptibilities in the saddle point regime of the hole-doped case with $t' = -0.3t$ and $\mu = -t$. The dashed lines in the left plot show the flow of Cooper couplings, the solid lines umklapp processes between the saddle points. The dotted line denotes the largest coupling in the BZ diagonal. In the right plot the solid line denotes the d-wave pairing susceptibility $\chi_{d-\rm wave}$, the dashed-dotted line the AF susceptibility $\chi_s(\pi, \pi)$.

as well but they are merely driven by the couplings between the saddle points and diverge less rapidly. These results are shown in Figure 7 and Figure 8. Starting the flow with purely repulsive interaction, the Cooper channel will initially always decrease the values of the Cooper scatterings. However if the FS is close to the saddle points the particle-hole channel with the rapidly growing umklapp processes also affects the large angle pair scattering processes which involve momentum transfer (π, π). In the saddle point regime of the hole-doped case this effect is stronger than the suppression through the Cooper channel and the large angle pair scattering processes grow upon reducing the energy scale which in turn enhances the flow of the small angle pair scattering to negative values. Similarly it can be also seen that the growth of the d-wave pair scattering enhances the flow of the umklapp (π, π) processes. In the saddle point regime with the FS close to the $(0, \pi)$ and $(\pi, 0)$-points this mutual reinforcement between d-wave and AF processes is very effective as it

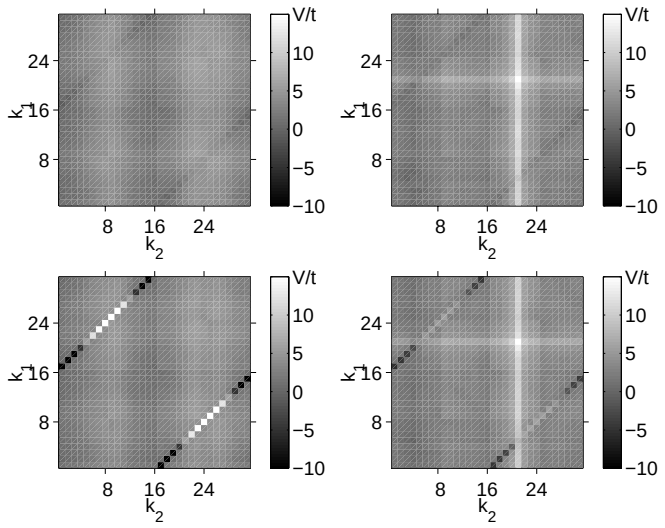

Fig. 9. Snapshot of the RG flow when the couplings have reached values larger than the bandwidth for the electron-doped case, $t' = -0.3t$, $T = 0$. For the upper two plots $\mu = -0.1t$ ($\langle n \rangle \approx 1.18$), and the FS intersects the US. The left plots show the dependence of the scattering vertex $V_\Lambda(k_1, k_2, k_3 = 1)$ with the first outgoing wavevector fixed at point 1 on the incoming wavevectors $\mathbf{k}_F(k_1)$ and on $\mathbf{k}_F(k_2)$ where k_i labels the positions of the points around the FS (see Fig. 5). In the upper right plot, $k_3 = 4$, *i.e.* the first outgoing wavevector is near the BZ diagonal. The sharp vertical repulsive feature at $k_2 = 21$ is due to nesting with the wavevector $\mathbf{k}_F(k_2) - \mathbf{k}_F(k_3) \approx (\pi, \pi)$. For the lower plots, $\mu = 0.04t$ ($\langle n \rangle \approx 1.22$) and the FS lies outside the US. The left plot again corresponds to $k_3 = 1$ and the right plot is for $k_3 = 4$. The diagonal features belong to Cooper processes with $\mathbf{k}_F(k_1) + \mathbf{k}_F(k_2) = 0$. The sign structure of the Cooper pair scattering reveals that the dominant pairing symmetry is $d_{x^2-y^2}$, *e.g.* $V_\Lambda(1, 17, 1)$ is attractive while $V_\Lambda(1, 17, 9)$ is repulsive.

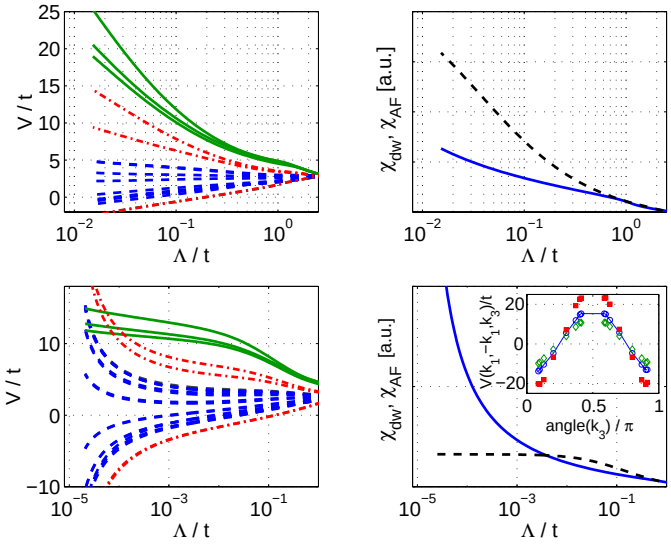

Fig. 10. Flow of coupling functions (left plots) and susceptibilities (right plots) in the crossover regime of the electron-doped case, $t' = -0.3t$ and $T = 0$. The upper plots correspond to $\mu = -0.1t$ where the FS intersects the US and the AF processes processes diverge at non-zero energy scale. The lower plots are for $\mu = 0.04t$, which is further away from half-filling. The dashed lines in the left plots show the flow of Cooper couplings at the FS, the solid lines umklapp processes in the BZ diagonal $V_\Lambda(4, 4, 21)$, $V_\Lambda(3, 4, 21)$, and $V_\Lambda(5, 4, 21)$. The dashed-dotted lines denote Cooper processes between the saddle point regions with band energies below the FS (discussed in the text). In the right plots the solid line denotes the d-wave pairing susceptibility and the dashed-dotted line the AF susceptibility $\chi_s(\pi, \pi)$. Note the logarithmic scale axis. The inset in the lower right plot shows the Cooper pair scattering $V(\mathbf{k}_1, -\mathbf{k}_1, \mathbf{k}_3)$ close to the instability as function of the angle of $\mathbf{k_3}$ around the FS. The filled squares (open diamonds) correspond to scattering between $\mathbf{k}$-space points below (above) the FS at band energy $\pm 0.8t$ while the circles connected by straight solid lines show the values at for pairs on the FS. $\mathbf{k}_1$ is at angle $\approx -\pi$ below (above) or on the FS (see Fig. 4).

only involves low-energy quasiparticles. Therefore d-wave and AF processes diverge together at a single high energy scale.

3.2 Flow in the electron-doped case

For the electron-doped side we again take $t' = -0.3t$. Here, unlike the hole-doped case, smaller absolute values of t' yield a similar picture, only the critical scales become larger due to the improved nesting. Half-filling corresponds to $\mu = -0.65t$. Upon increasing μ and $\langle n \rangle$, the FS crosses the US close to the BZ diagonals until $\mu = 0t$ and then loses contact to the US if we further increase the particle number. At these densities the flow to strong coupling changes drastically, therefore we concentrate on this filling range. In Figure 10 we show the flow to strong coupling for two different chemical potentials: in the upper plots $\mu = -0.1t$ and the FS intersects the umklapp surface close to the BZ diagonals. Here the dominant processes which become large at comparably high energy scales are umklapp processes between the BZ diagonals involving the momentum transfer (π, π) (see solid lines in Fig. 10 and the sharp features in Fig. 9).

The Cooper processes between particles at the FS have dominant $d_{x^2-y^2}$-symmetry but remain of the order of the bandwidth even when we integrate the flow far out of the perturbative range. Thus the coupling to the strongly growing AF processes is only weak, as expected from the location of the FS. Consequently the characteristic energy scales where AF and d-wave channels start to grow are very different, in strong contrast to the saddle point regime of the hole-doped case. Nonetheless we can still find signs of a coupling between d-wave and AF channel: if we consider Cooper processes for particles at the saddle points below the FS we find a much stronger growth towards lower scales (see dashed-dotted lines in Fig. 10). A large angle Cooper pair scattering between two inequivalent saddle points involves momentum transfer $\approx (\pi, \pi)$ and is therefore enhanced by the AF processes. But unlike the saddle point regime in the hole-doped case, the

k-space regions where the coupling occurs are away from the FS and therefore there is only a weak influence of this mechanism on the true low-energy excitations. One should also note that in more realistic calculations including self-energy effects the coupling through off-FS processes will be further reduced by the short lifetimes of the quasiparticles in these regions.

Increasing the band filling such that the FS loses its intersection with the US, the umklapp and other (π,π)-processes in the diagonals get cut off and saturate at low scales (see solid lines in the lower left plot of Fig. 10). Thus the d-wave Cooper processes can finally diverge at very low scales (at least two orders of magnitude lower than in the previous case). The Cooper pair scattering is shown in the inset of Figure 10. Again the off-FS d-wave Cooper processes closer to the saddle points benefit more from the AF scattering processes and grow more strongly than the Cooper processes for pairs at the FS, but this difference becomes less with increasing particle density away from half-filling. Apart from this side-effect we emphasize that in this low-scale d-wave regime only Cooper processes diverge. Umklapp and and nesting processes are cut off and do not develop singularities.

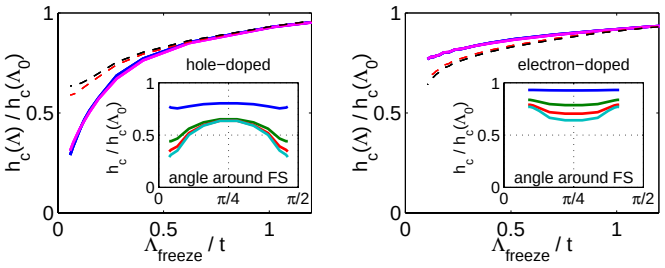

Fig. 11. Flow of the coupling of quasiparticles at different points on the FS to uniform external charge fields, normalized to the values with the bare interactions $U = 3t$. The left plot corresponds to the saddle-point regime of the hole-doped case $\mu = -t$, $T = 0.04t$, while the right plot shows data for the electron-doped case $\mu = -0.1t$, $T = 0.01t$. The solid lines are for **k**-points on the FS in the vicinity of the saddle points, the dashed lines for **k**-points on the FS in the BZ diagonal. $\Lambda_{\rm freeze}$ is the energy scale down to which the flow of the coupling function is taken into account. Below $\Lambda_{\rm freeze}$ the coupling functions are kept constant. The insets show the angular variation along the FS for different values of $\Lambda_{\rm freeze}$.

4 Flow of the susceptibilities

Next we compare the flow of various susceptibilities. First we analyze the real parts of the static d-wave pairing susceptibility $\chi_{d-\rm wave}$ and the AF susceptibility $\chi_s(\pi,\pi)$. Moreover, as a kind of cross-check, we analyze the coupling to uniform static charge and spin fields for electrons at different points on the Fermi surface.

In the saddle point regime of the hole-doped case the overall behavior of these probes together with general features of the RG flow of the couplings indicated the tendency towards formation of an insulating spin liquid: both $\chi_{d-\rm wave}$ and $\chi_s(\pi,\pi)$ diverge together in a similar way (see Fig. 8) and in view of the mutual reinforcement between both channels it is very plausible that the strong coupling state will incorporate both types of fluctuations. On the other hand the coupling of the saddle point regions to uniform charge and spin fields becomes increasingly suppressed in the RG flow (the charge couplings are shown in the left plot in Fig. 11), suggesting the opening of charge and spin gaps around the saddle points. In contrast to that the charge coupling for quasiparticles in the BZ diagonals does not renormalize to zero. This anisotropic flow is consistent with a truncation of the FS at the saddle points while the BZ diagonals remain metallic. The flow of the scattering rates described in Section 6 corroborates this scenario.

In the electron-doped case the situation is rather different. Since d-wave and AF channel do not couple strongly the corresponding susceptibilities have very different flows. While $\chi_s(\pi,\pi)$ already grows considerably at higher scales and eventually diverges if the system is not far away from half filling, $\chi_{d-\rm wave}$ becomes large only at low scales. We therefore expect that the system will have only two different phases if we allow for a sufficient amount of 3D coupling: one AF phase with higher critical scale and temperature, and, if we increase the band filling such that the instability in the latter channel becomes cut off by the FS curvature, a rapid drop in the energy scale with a low-T Kohn-Luttinger-type d-wave phase. This – compared to the saddle point regime – more conventional picture is also supported by the behavior of the uniform susceptibilities and the k-space dependence of the coupling to the corresponding external fields: the coupling to uniform charge fields (see right plot in Fig. 11) is not strongly suppressed, *i.e.* there are no pronounced indications for incompressible or truncated parts of the FS in our weak-coupling analysis. The reduction of the charge couplings becomes even weaker when the filling is increased. In contrast to the hole-doped case the strongest suppression now occurs for wavevectors in the BZ diagonals, in agreement with the fact that Umklapp processes flow most strongly there (see inset in the right plot of Fig. 11). Again this type of anisotropy compares well the angular-dependent quasiparticle lifetimes obtained with the RG calculations described below and FLEX (fluctuation exchange approximation) [17].

5 Tentative phase diagram for the electron-doped case

The tentative phase diagram for the hole-doped Hubbard model extracted from the one-loop flow to strong coupling was discussed in [10]. Here present a schematic phase diagram for the electron-doped side.

Generally with this type of calculations it is difficult to determine exact phase boundaries, *e.g.* the parameters where the ground state changes from AF to d-wave superconducting long range order. Nor can we actually prove the existence of the phases suggested by one-loop flow. Self-energy and higher order effects will become large once

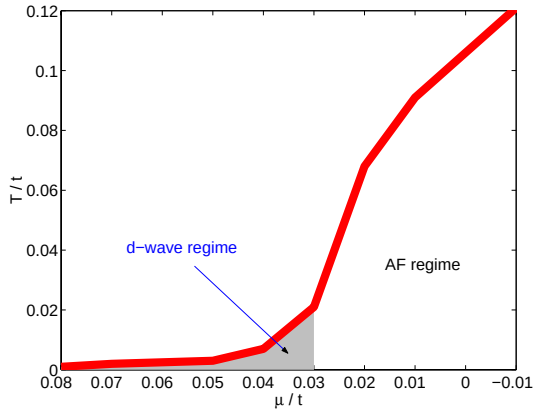

Fig. 12. Dependence of the flow to strong coupling on μ and T in the electron-doped regime for $t' = -0.3t$ and $U = 3t$. The thick line denotes the critical temperature above which we can integrate down to $\Lambda = 0$ with all couplings remaining smaller than $15t$. In the d-wave dominated regime $\chi_{d-\mathrm{wave}}$ grows stronger, while in the AF regime $\chi_s(\pi,\pi)$ dominates (the precise criteria are given in the text). For the displayed values of μ the electron-doping varies between 0.2 ($\mu = -0.1t$) and 0.23 ($\mu = 0.08t$).

the coupling functions exceed the order of the band width and from the flow below that scale it is impossible to tell whether the different classes of couplings really diverge or not. Similarly fluctuations around possible ordered states are not taken into account properly. Nevertheless since in the electron-doped case we observe two different tendencies which are weakly coupled and dominate on opposite sides of the considered density range, we can well discriminate between distinct regimes with different dominant fluctuations. If long range order is possible (at $T = 0$ or at finite T if we add some degree of three-dimensional coupling), its type will most probably correspond to the dominant fluctuations visible in the one-loop RG. Bearing in mind these remarks, we present a schematic phase diagram for the case $t' = -0.3t$ and initial $U = 3t$ in Figure 12. For chemical potential $\mu < 0.03t$ (which corresponds to $\langle n \rangle \approx 1.21$ per site) we find an AF dominated instability with comparably high critical temperature T_c (above T_c we can integrate down to $\Lambda = 0$ with all couplings staying smaller than $15t$.). For larger chemical potential the instability is d-wave dominated. The criterion we used for the distinction was the derivative of $\chi_{d-\mathrm{wave}}$ and $\chi_s(\pi,\pi)$ with respect to Λ when the maximal coupling grows larger than $12t$. We repeat that this distinction does not allow any quantitative predictions for the true phase diagram. In particular the critical scales and temperatures for the d-wave phase strongly depend on the criterion used to separate the regimes[1].

[1] If we chose to compare the susceptibilities at higher values of the couplings, *i.e.* $20t$ instead of $12t$, the d-wave phase would extend further to smaller electron-dopings (to approx. $\mu = 0.01t$). Very close to the instability however, when the coupling function becomes huge, our one-loop RG scheme cannot be justified.

In the electron-doped case considered here there are two disparate energy scales. The first one, which can be high close to half filling, is related to the AF-(π,π) processes between the BZ diagonals. The second energy scale is given by the critical scale of the d-wave Cooper channel and remains much lower close to half-filling. Only if the AF energy scale becomes too low at increased doping, when the FS curvature prevents a real flow to strong coupling of the AF processes, an instability in the d-wave Cooper channel can occur. In the present case, the crossover energy scale is mainly determined by the particle density which regulates the overlap of the FS with the US, *i.e.* the low energy phase space available for elastic scattering with momentum transfer (π,π). A qualitatively similar picture was found by Manske *et al.* [18] who solved the generalized Eliashberg equations with a spin-fluctuation induced pairing interaction obtained within a FLEX scheme.

As mentioned above, on the electron-doped side the flow to strong coupling is qualitatively similar for all $t' < 0$, only the critical scales and relative widths of the regimes change. Thus for band fillings larger than one particle per site our observations for $t' = -0.3t$ are in full qualitative agreement with the results of Zanchi and Schulz [6] for $t' = 0$ and Halboth and Metzner [8,9] for smaller absolute values of the next-nearest neighbor hopping t'. In particular in the analysis of reference [9] the d-wave channel becomes dominant roughly when the FS loses its intersection with the US upon increasing the electron density.

6 Scattering rates

6.1 Hole-doped case

Here we describe our results for the quasiparticle scattering rates in the hole-doped case. There we are mainly interested in electron densities corresponding to the saddle point regime [10] briefly described above, because there the flow to strong coupling becomes qualitatively different from the d-wave superconducting instability at lower densities. Again, since we cannot prove the FS truncation suggested by the flow in the saddle point regime, our main goal is to analyze whether the behavior of the scattering rates is consistent with this scenario.

Typical results for the scattering rates in the saddle point regime ($\mu = -1.1t$) above the critical temperature obtained with the method described in Section 2.2 are shown in Figure 13. The temperature was chosen such that the couplings V_Λ do not become too large when we integrate the flow to $\Lambda = 0$, for the lowest T shown the maximum coupling reaches $\approx 11.5t$. This is already larger than the bandwidth, but this high value is only reached at low scales and most couplings remain smaller. Therefore the results should be qualitatively correct. An anisotropy in the scattering rate is clearly observable but not too pronounced, the maximum ratio between $\mathrm{Im}\,\Sigma$ at the saddle points and in the diagonals at $\pi/4$ is ≈ 2. The temperature dependence of $\mathrm{Im}\,\Sigma(\mathbf{k}_F, \omega = 0)$ is shown in Figure 13 for $\mu = -1.1t$ which is above the saddle point regime and

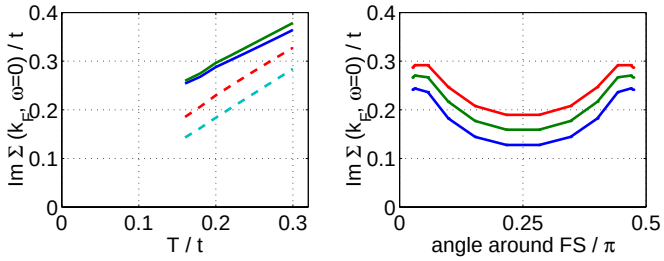

Fig. 13. Left: Temperature dependence of imaginary part of the self-energy at four different positions on the FS for the hole-doped case with $\mu = -1.1t$ and $t' = -0.3t$. The dashed lines belong to points in the BZ diagonal, the solid lines to points closer to the saddle points. Right: Imaginary part of the self-energy *versus* angle around the FS in the saddle point regime at $\mu = -1.1t$ for different temperatures above the instability. The lower line (circles) corresponds to $T = 0.15t$, the middle line (diamonds) to $T = 0.18t$ and the upper line is at $T = 0.21t$. For $T = 0.15t$ the largest coupling at $\Lambda = 0$ is $\approx 11.5t$, for $T = 0.21t$ they reach $\approx 8.9t$. The saddle points are at angles 0 and $\pi/2$.

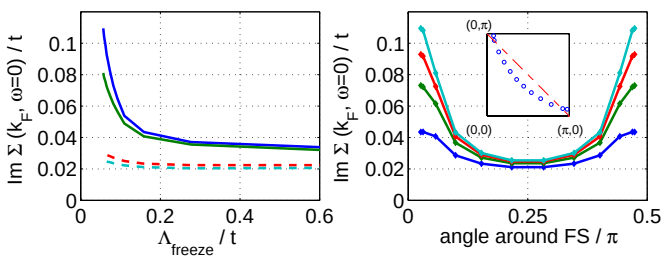

Fig. 14. Left: Change of the scattering rate through the flow of the interactions V_Λ for different positions on the Fermi surface in the hole-doped case, calculated on a 48×3 system. $\Lambda_{\rm freeze}$ is the scale below which the interactions are kept constant. Right: Angular variation of $\mathrm{Im}\,\Sigma(\mathbf{k}_{\rm F}, \omega = 0)$ with $\mathbf{k}_{\rm F}$ varying on the FS from one to the next saddle point. The different lines shows $\Sigma(\mathbf{k}_{\rm F}, \omega = 0)$ with the couplings stopped at $V_{\Lambda,\max} = 6t$ (bottom line), $9t$, $12t$ and $15t$ (top line). The inset shows the 12 points on a quarter of the FS. For both plots $\mu = -1.1t$ and $T = 0.04t$ corresponding to the saddle point regime.

close to the van Hove doping at $\mu = -1.2t$. All curves for the different positions on the Fermi surface show an almost linear increase with T. Both, the angular variation and the temperature dependence, are qualitatively consistent with the ARPES results by Valla *et al.* [15][2]. In comparison with the model assumptions in [13] we note that our calculations at temperatures above the flow to strong coupling yield a smaller anisotropy in the scattering rates and no T^2 behavior for the quasiparticles in the BZ diagonal. Our data resemble more FLEX results obtained by Kontani *et al.* [17] Altmann *et al.* [19]. The first group was able to describe resistivity and Hall coefficients in qualitative agreement with the experiments. For high temperatures the qualitative similarity between FLEX calculations and our RG analysis is not accidental because for $T > T_{\rm c}$ when the flow does not diverge, the main scattering occurs in the (π, π) spin fluctuation channel which the typical FLEX schemes focus on.

From a theoretical point of view the linear-T dependence is not unexpected because already the bare two-loop diagram with unrenormalized couplings yields this behavior if the band filling is sufficiently close to the van Hove filling [20,21]. Hence it should be considered as an effect of the van Hove singularities and does not immediately imply a breakdown of the quasiparticle concept.

For lower temperatures the coupling function flows to strong coupling at a non-zero critical scale $\Lambda_{\rm c}$. Therefore we cannot integrate the flow down to zero scale and do not obtain a good approximation for $\mathrm{Im}\,\Sigma$ with the above method. At $\Lambda_{\rm c}$ the selfenergy diverges together with the couplings and we expect that the quasiparticles will be at least partially destroyed. Although we cannot really access this strong coupling region, we can gain some insight on how this quasiparticle destruction takes place by considering the change in the two-loop selfenergy through the flow of the coupling function. The results for $\mu = -t$ and $T = 0.04t$ are shown in Figure 14. If we freeze the flow of the four point vertices V_Λ already at high scales, we basically obtain the bare two-loop selfenergy when we integrate the RG equation for the selfenergy down to $\Lambda = 0$. There, the anisotropy between saddle point regions and BZ diagonals is small. If we now subsequently include the flow of V_Λ by reducing $\Lambda_{\rm freeze}$, the scattering rate for quasiparticles around the saddle points grows strongly. For the quasiparticles in the BZ diagonals the scattering rate is not much affected by the flow of the couplings. Thus the flow of the scattering rates for these values of the band filling is consistent with a breaking up of the FS into two distinct regions, as suggested in [10] based on an analysis of the flow of the coupling function and susceptibilities: around the saddle points, the quasiparticles are subject to divergent scattering processes, there we also found the strong suppression of the charge compressibility. In the BZ diagonals which appeared to remain compressible, the scattering rate stays in the weak coupling range, consistent with the FS remaining untruncated in these regions.

When the band filling is increased further towards half-filling the energy and temperature scale for the flow to strong coupling rises and the anisotropy of the scattering rates at temperatures above this flow to strong coupling becomes weaker. The reason is that the scattering processes between the saddle point regions lose their dominant role, and the strongest scattering processes occur between FS parts connected by (π, π), now closer to the BZ diagonals.

6.2 Electron-doped case

In Figure 15 we show the results for the electron-doped case obtained at higher temperatures where the flow does

[2] Valla *et al.* [15] find a leveling off of the scattering rate very close to the saddle points at lowest T in the normal state, which is not present in our results. If this is an intrinsic effect of the CuO_2-planes, it may be beyond our weak coupling calculation.

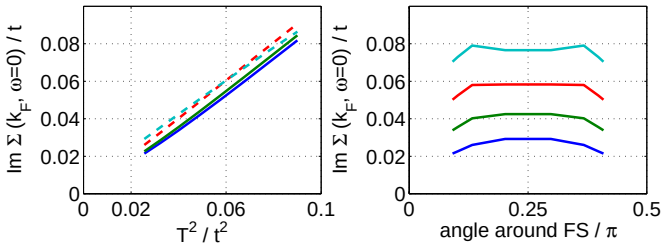

Fig. 15. Left: Temperature dependence of imaginary part of the selfenergy at four different positions on the FS for the electron-doped case. The dashed lines belong to points in the BZ diagonal, the solid lines to points closer to the saddle points. Right: Angular variation of $\mathrm{Im}\,\Sigma(\mathbf{k}_\mathrm{F}, \omega = 0)$ with $\mathbf{k}_\mathrm{F}$ varying on the FS from one to the next saddle point. The different lines show $\Sigma(\mathbf{k}_\mathrm{F}, \omega = 0)$ at different temperatures from $T = 0.16t$ (bottom line) to $T = 0.28t$ (top line). The results in both plots were obtained using a 32×3 system with $t' = -0.3t$ and $\mu = 0$.

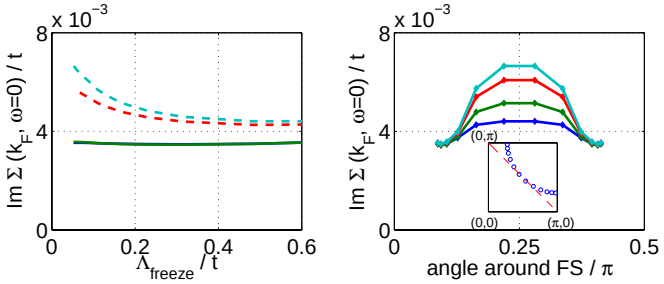

Fig. 16. Left: Change of the scattering rate through the flow of the interactions V_Λ for different positions on the Fermi surface in the electron-doped case. Λ_freeze is the scale below which the interactions are kept constant. Right: Angular variations of $\mathrm{Im}\,\Sigma(\mathbf{k}_\mathrm{F}, \omega = 0)$ with $\mathbf{k}_\mathrm{F}$ varying on the FS from one to the next saddle point. The different lines shows $\Sigma(\mathbf{k}_\mathrm{F}, \omega = 0)$ with the couplings stopped at $V_{\Lambda,\max} = 6t$ (bottom line), $9t$, $12t$ and $15t$ (top line). The inset shows the 12 points on a quarter of the FS. For both plots $\mu = -0.1t$ and $T = 0.04t$.

not exceed the order of the bandwidth. There are striking differences compared to the results obtained in the hole-doped saddle point regime. First the overall magnitude of $\mathrm{Im}\,\Sigma(\mathbf{k}_\mathrm{F}, \omega = 0)$ at a given temperature is much smaller, almost by an order of magnitude. We attribute this to the reduced density of states around the FS, the van Hove singularities are far away from the FS. Second the temperature dependence of the scattering rates is far from being linear and appears to be roughly consistent with a T^2-behavior at low temperatures above the flow to strong coupling[3]. The data for $\mathbf{k}$-points in the BZ diagonal do not extrapolate to 0 for $T \to 0$ due to the increase of the coupling function at lower T. Further, the anisotropy of the scattering rate is different and much weaker than in the hole-doped case. The FS parts which feel the strongest scattering at lower T are now in the BZ diagonal (see right plot in Fig. 15 for angular dependence). This is consistent with the flow of the interactions which grow fastest in these regions. Our results also agree qualitatively with FLEX calculations [17,19], which show that the in the electron-doped case the "hot spots" with the shortest quasiparticle-lifetime move towards the BZ diagonal. Nonetheless due to the weakness of the anisotropy the data do not suggest a truncation of the FS like in the hole-doped case. This can be also seen at lower temperatures (see Fig. 16), where flow of the scattering rates remains comparably weak when the coupling function flows to strong coupling.

7 Discussion

We have presented N-patch RG results for the two-dimensional t-t' Hubbard model with particle density $n > 1$ per site and $t' = -0.3t$. We have shown that the RG flow to strong coupling is qualitatively different from the $n < 1$ case because of the different location of the FS in both cases. The saddle-point regime [10] which we associated with the pseudogap state in the (hole-)underdoped cuprates is absent in our RG study of the electron-doped side. Instead the picture closely resembles the observations made by Zanchi and Schulz [6] and Halboth and Metzner [8,9] for zero or smaller absolute value of the next-nearest neighbor hopping t'. Upon increasing the electron density we find a rapid decrease of the critical scale for the instability where the flow of the otherwise strongly growing AF susceptibility is cut off. This leaves a small window for a Kohn-Luttinger-type $d_{x^2-y^2}$-wave instability at lower scales and temperatures. The tendency towards incompressibility and truncation of parts of the FS is weaker than in the hole-doped case and strongest in the BZ diagonal. At temperatures above the strongly coupled phase we find slightly anisotropic scattering rates with strongest scattering of quasiparticles, *i.e.* "hot spots" in the BZ diagonal. The temperature dependence of the scattering rates is roughly quadratic.

Indeed the experimental phase diagram of the electron-doped cuprates shows a relatively wide AF phase with a boundary to superconducting phase with lower critical temperature. There is increasing experimental evidence [24–27] that the pairing symmetry of this phase is $d_{x^2-y^2}$. Moreover the in-plane resistivity in the normal state shows a quadratic temperature dependence [28,29].

Note that in our RG study the difference between the energy scales characteristic to these phases is considerably larger than the experimental values. However one should keep in mind that our one-loop analysis can only provide a qualitative picture for the understanding of the real materials. In particular we cannot make any predictions about the stability of the phases suggested by the RG flow and the precise location of the transition from AF to d-wave regime. In fact the Fermi surface in $Nd_{1.85}Ce_{0.15}CuO_4$ with a superconducting T_c of $24K$ seen by ARPES [27] still intersects the Umklapp surface. Thus it might be that

[3] In an isotropic two-dimensional Fermi liquid, we expect $\mathrm{Im}\,\Sigma(\omega = 0, \mathbf{k}_\mathrm{F}) \sim (T/T_\mathrm{F})^2 \log(T_\mathrm{F}/T)$ [22,23]. Since our calculations are rather qualitative we do not attempt a detailed comparison of the data with this T-dependence.

our criterion for the transition from AF to d-wave regime overestimates the width of the AF regime.

The saddle point regime in the hole-doped case with the diverging umklapp processes was interpreted as a precursor of the Mott state where the FS becomes truncated at the saddle points [10]. The anisotropic scattering rates described above, which grow strongest at the saddle points as the flow goes to strong coupling, are consistent with this scenario. Due to the location of the FS the diverging umklapp processes also generate strong d-wave pairing correlations. In this situation the d-wave-paired condensate which may form at sufficiently low temperature will still be subject to the umklapp scattering at the saddle points where the FS becomes truncated. This may result in a reduced superfluid weight arising from the open parts of the FS in the BZ diagonals only.

In the electron-doped case the umklapp and other AF processes predominantly occur between the BZ diagonals and do not strongly drive the d-wave correlations, they can only lead to a rapid growth of AF correlations. Thus, instead of being strongly coupled and mutually reinforcing each other in the flow, AF and d-wave channel have disparate characteristic energy scales and influence each other only weakly. As soon as the umklapp processes in the BZ diagonals flow to strong coupling, the instability is entirely dominated by AF correlations because the energy scale of the d-wave instability is much lower. This implies that coming from the electron-overdoped side the precursors of the Mott state only occur in the AF phase and should have less influence on the d-wave state. In particular we speculate that in the superconducting state all electrons contribute to the superfluid weight in contrast with the hole-(under)doped case.

It is a pleasure to thank T.M. Rice, M. Salmhofer, U. Ledermann, K. Lehur, M. Zhitomirsky, R. Hlubina and D. Vollhardt for stimulating discussions. The Swiss National Science Foundation is acknowledged for financial support. The numerical calculations were performed on the *Asgard* Beowulf cluster of ETH Zürich.

References

1. P.W. Anderson, *The Theory of Superconductivity in the High-T_c Cuprates* (Princeton University Press, 1997).
2. For a review see: D.J. Scalapino, J. Low Temp. Phys. **117**, 179 (1999).
3. I. Dzyaloshinskii, Sov. Phys. JETP **66**, 848 (1987); I. Dzyaloshinskii, J. Phys. I, France **6**, 119 (1996).
4. H.J. Schulz, Europhys. Lett. **4**, 609 (1987).
5. P. Lederer, G. Montambaux, D. Poilblanc, J. Phys. **48**, 1613 (1987).
6. D. Zanchi, H.J. Schulz, Europhys. Lett. **44**, 235 (1997); D. Zanchi, H.J. Schulz, Phys. Rev. B **61**, 13609 (2000).
7. N. Furukawa, T.M. Rice, M. Salmhofer, Phys. Rev. Lett. **81**, 3195 (1998).
8. C.J. Halboth, W. Metzner, Phys. Rev. B **61**, 7364 (2000).
9. C.J. Halboth, W. Metzner, Phys. Rev. Lett. **85**, 5162 (2000).
10. C. Honerkamp, M. Salmhofer, N. Furukawa, T.M. Rice, Phys. Rev. B **63**, 35109 (2001).
11. Shan-Wen Tsai, J.B. Marston, `cond-mat/0010300`.
12. M.P.A. Fisher, in *Topological aspects of low-dimensional systems*, edited by A. Comtet *et al.*, Les Houches LXIX (EDP Sciences & Springer, Paris, 1998), `cond-mat/9806164`, and references therein.
13. L.B. Ioffe, A.J. Millis, Phys. Rev. B **58**, 11631 (1998).
14. R. Hlubina, Phys. Rev. B **58**, 8240 (1998).
15. T. Valla, A.V. Federov, P.D. Johnson, Q. Li, G.D. Gu, N. Koshizuka, Phys. Rev. Lett. **85**, 828 (2000).
16. M. Salmhofer, C. Honerkamp, Prog. Theor. Physics **105**, 1 (2001); for a related formalism, see also M. Salmhofer, *Renormalization: An Introduction; Texts and Monographs in Physics* (Springer, 1999).
17. H. Kontani, K. Kanki, K. Ueda, Phys. Rev. B **59**, 14723 (1999). See also H. Kontani, `cond-mat/0011327`.
18. D. Manske, I. Eremin, K.H. Bennemann, Phys. Rev. **62**, 13922 (2000).
19. J. Altmann, W. Brenig, A.P. Kampf, `cond-mat/9707267` (unpublished).
20. P.A. Lee, N. Read, Phys. Rev. Lett. **58**, 2691 (1987).
21. G. Kastrinakis, Physica C **318**, 497 (2000); Physica C **340**, 119 (2000).
22. A.V. Chaplik, Sov. Phys. JETP **33**, 997 (1971).
23. C. Hodges, H. Smith, J.W. Wilkins, Phys. Rev. B **4**, 302 (1971).
24. C.C. Tsuei, J.R. Kirtley, Phys. Rev. Lett. **85**, 182 (2000); Rev. Mod. Phys. **72**, 969 (2000).
25. R. Prozorov, R.W. Giannetta, P. Fournier, R.L. Greene, Phys. Rev. Lett. **85**, 3700 (2000).
26. A. Mourachkine, Europhys. Lett. **50**, 663 (2000).
27. N.P. Armitage, D.H. Lu, D.L. Feng, C.Kim, A. Damascelli, K.M. Shen, F. Ronning, Y. Onose, Y. Taguchi, Y. Tokura, Z.-X. Shen, Phys. Rev. Lett. **86**, 1126 (2001).
28. C.C. Tsuei, A. Gupta, G. Koren, Physica C **161**, 415 (1989).
29. J.L. Peng, E. Maiser, T. Venkatesan, R.L. Greene, G. Czjzek, Phys. Rev. B **55**, R6145 (1997).